SPECT STUDY RESTORATION USING ANATOMICAL AND GEOMETRICAL CONSTRAINTS EXTRACTED FROM MRI IMAGES

S. Benameur[‡], *M. Mignotte*[‡], *J.-P. Soucy*[†], *and J. Meunier*[‡]

[‡] Département d'Informatique et de Recherche Opérationnelle (DIRO), Université de Montréal,
CP 6128, Station Centre-Ville, P.O. 6128, Montréal (Québec), Canada, H3C 3J7
[†] Centre Hospitalier de l'Université de Montréal,
1560 rue Sherbrooke est, Montréal (Québec), Canada, H2L 4M1
E-MAIL: BENAMEUS@IRO.UMONTREAL.CA

Address for correspondence

Said BENAMEUR

Université de Montréal,

Département d'Informatique et de Recherche Opérationnelle (DIRO),

Pavillon André-Aisenstadt, 2920, chemin de la Tour,

Montréal (Québec), Canada, H3T 1J4

Phone: (514) 343-2264

Fax: (514) 343-5834

E-MAIL: BENAMEUS@IRO.UMONTREAL.CA

SPECT study restoration using anatomical and geometrical constraints extracted from MRI images

ABSTRACT

Brain SPECT imaging of regional cerebral blood flow distribution (rCBF) is a well established functional imaging method which is widely used in a variety of clinical and research settings for the assessment of normal and abnormal neurological function. However, in part because of the scattering of emitted photons inherent to this imaging process, amongst others causes, brain SPECT images generally exhibit poor spatial resolution and low signal-to-noise ratio. This leads to substantial errors in measurements of regional brain radioactivity concentrations, making difficult to come up with reliable, accurate and objective observations. In order to improve the resolution of these images and therefore to facilitate their interpretation, we herein propose an original extension of the NAS-RIF deconvolution technique of Kundur and Hatzinakos [1]. That extension allows the reconstruction process to be constrained by anatomical and geometrical information extracted from a high resolution anatomical procedure such as magnetic resonance imaging (MRI). It also has the advantage of efficiently incorporating, within the NAS-RIF method, a regularization term which stabilizes the inverse solution. In our application, this anatomical-based regularization term uses the result of an unsupervised Markovian segmentation obtained after a preliminary registration step between the MR and SPECT data volumes obtained from the same patient. This method has been successfully tested on 30 pairs of brain MRI and SPECT acquisitions from different subjects and on Hoffman and Jaszczak SPECT phantoms. The experiments reported in this paper demonstrate that the discussed method performs better, in terms of signal-to-noise ratio, than a classical supervised restoration approach using a Metz filter. Also, this method enhances contrast of the SPECT restored images with little increase in mottle.

Index Terms: *SPECT imagery, MR imagery, 3D blind deconvolution, unsupervised segmentation, Markov Random Field model, 3D/3D registration, image restoration, information fusion.*

1. INTRODUCTION

The spatial resolution and signal-to-noise ratio displayed by brain single photon emission computed tomography (SPECT) images is rather limited, when compared with that from other functional (PET, fMRI) or anatomical techniques (MRI, CT scanning). This fact limits the potential use of brain SPECT images. For instance, it is not easy to differentiate low tracer uptake due to a functional deficit, where brain tissue still is anatomically intact, from low uptake generated by focal atrophy, where tissue is lost and replaced by cerebrospinal fluid (CSF) [2].

Several methods have been proposed to improve the spatial resolution of SPECT images. These methods can be split into two major classes, namely methods including restoration techniques during or after the reconstruction process from projections.

Amongst the first class of such methods, we can cite the Bayesian tomographic reconstruction techniques. These methods statistically incorporate, into the tomographic reconstruction problem, both noise model and *a priori* knowledge about the types of reconstruction results acceptable as estimates of the actual spatial distribution of activity. For those approaches, in order to avoid (to some extent) over-smoothing of edges and details, some priors have been specifically proposed for SPECT. Among them, we can cite the generalized Gaussian Markov random field prior model [3]. This model includes a Gaussian MRF and an absolute-value potential function which varies according to the value of an internal parameter, which in fact controls the degree of smoothness of the reconstruction and/or the sharpness of the edges to be formed in the reconstructed image. We can also mention the median prior term, proposed by Alenius *et al.* in [4] where a penalty term is set according to the deviance of a pixel from the local median, allowing for both noise reduction and edge preservation.

One way to improve the spatial resolution of the SPECT images (during the reconstruction process) consists in taking into account the scatter effect inherent to this imaging process *via*, for example, a point spread function including all collimator and detector effects. To this end several algorithm for scatter compensation in brain SPECT have been proposed in the literature [5, 6, 7, 8, 9, 10]. Another way consists in taking into account the distance-dependent collimator blurring and, at a smaller extent, the intrinsic detector resolution. To this end, a successful correction method, using the frequency-distance principle [11] [12] has been proposed. Another approach

is the direct incorporation of the collimator blurring in the reconstruction process by using "Gaussian-diffusion" [13] (allowing to obtain the appropriate blurring with small convolution kernels). A comparison between these two strategies has been reported in [14].

A second way to accurately model and include the prior information concerning the spatial properties (anatomy) of the actual brain volume being imaged by SPECT that has also been proposed utilises the registration of (high resolution) anatomical (CT or MR) images with the (low resolution) functional (SPECT or PET) images from the same patient. In these models [15, 16, 17, 18], prior anatomical information (i.e., structural information on the presence and location of important anatomical "landmarks" such as local discontinuities or the presence of extended homogeneous regions as seen for instance on an MR anatomical image) is incorporated into the tomographic reconstruction process in order to rightly constrain the reconstructed image and thus to improve its spatial resolution. These models usually express that, within a detected and segmented "uniform" anatomical region, neighboring pixels in the functional image tend to have similar grey level values (local homogeneity) or follow a Gaussian distribution with a unique mean value (global homogeneity) [19, 20, 21].

A second class of methods includes restoration or deconvolution techniques used after the reconstruction process. In this category, we can cite [22] where Rajabi *et al.* compared four widely used filters (i.e., Hanning, Butterworth, Metz and Wiener) in myocardial Tc99m-sestamibi SPECT studies. In [23] a non-negativity and support constraints recursive inverse filtering (NAS-RIF) algorithm proposed by Kundur and Hatzinakos [1], was extended to the 3D SPECT imaging restoration context. The NAS-RIF blind deconvolution technique is relevant to any situations in which an object of finite extend is imaged against a uniformly grey (or noisy) background [1]. This method can thus be efficiently exploited in brain SPECT imaging since the true undistorted rCBF map of a human brain consists of a finite support imaged against a noisy background (the background being secondary to the Poisson noise phenomenon inherent to imaging with radioactive elements; other sources of background in the images do not concern the inherent Poisson noise from the actual spatial distribution of radioactivity). The only information required for this deconvolution procedure is the non-negativity of the true image and the support of the object to be restored. In [23], this support was accurately determined by an unsupervised 3D Markovian segmentation technique applied to the SPECT volume.

In this paper, we propose to extend the method presented in [23] by introducing, into the NAS-RIF algorithm, a new spatially-adaptive regularization term for SPECT image deconvolution. This regularization term allows to efficiently include anatomical and geometrical information extracted from a high resolution anatomical MR image [24] while stabilizing the solution of the NAS-RIF inverse filter by preventing noise amplification and ringing artifacts. In our application, this anatomical-based regularization term exploits the result of an unsupervised Markovian segmentation obtained after a preliminary registration step between the MR and SPECT volume coming from the same patient. In our context, the proposed regularization term is quadratic and the NAS-RIF procedure thus involves recursive filtering of the degraded image to minimize a newly convex objective cost function. A conjugate gradient-based optimization is then used to minimize this cost function. This method will be tested on 30 pairs of brain MR and SPECT images from different patients and on Hoffman and Jaszczak SPECT Phantoms and compared with a classical supervised deconvolution/restoration approach using a classical Metz filter.

This paper is organized as follows. The section 2 briefly describes the proposed 3D anatomical constraint version of the NAS-RIF deconvolution technique. In section 3, we describe the registration and segmentation algorithms. The section 4 presents the validation protocol of the new restoration method. We then show some of our experimental results on a phantom and real brain SPECT volumes and validate the proposed model in section 5. Finally, we conclude in section 6.

2. 3D ANATOMICAL CONSTRAINT NAS-RIF ALGORITHM

2.1. 3D extended version of the NAS-RIF

In our application, and as proposed in [23], we will assume that 3D SPECT images are degraded by the following, classical linear model

$$g(x,y,z) \;=\; f(x,y,z) * h(x,y,z) + n(x,y,z) \tag{1}$$

in which $g(x,y,z)$, $f(x,y,z)$, and $h(x,y,z)$, denote respectively the degraded 3D image, the true image and the point spread function (PSF). $n(x,y,z)$ represents the additive noise and $*$ designates the 3D discrete linear convolution operator. The 3D blind deconvolution problem

consists then in determining $f(x,y,z)$ and $h(x,y,z)$ (or its inverse) given the blurred observation $g(x,y,z)$.

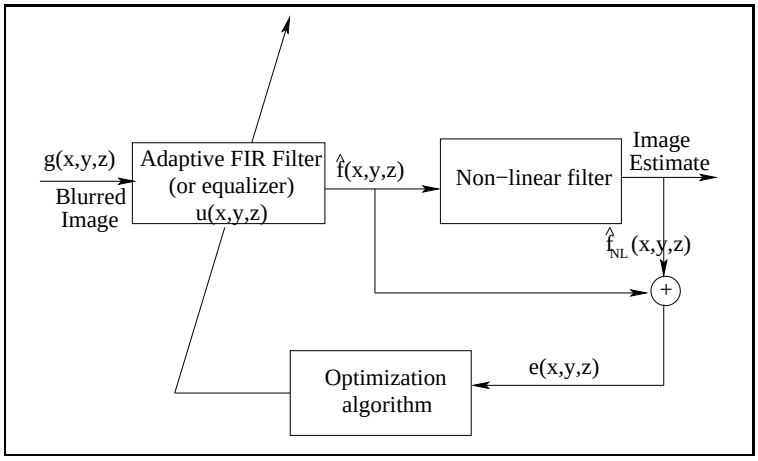

Figure 1: *Three-dimensional extension of the NAS-RIF deconvolution algorithm [1].*

In the 3D extended version of the NAS-RIF deconvolution strategy (cf. Fig. 1), the output of the FIR filter $u(x,y,z)$ of dimension $N_{xu} \times N_{yu} \times N_{zu}$ gives an estimate of the true image $\hat{f}(x,y,z)$. Each resulting estimation is passed through a nonlinear filter which uses a non-expansive mapping to project the estimated 3D image into the space representing the known characteristics of the true image (expressing in fact that the image is assumed to be non-negative with a known support). The difference between this projected image $\hat{f}_{\mathrm{NL}}$ and $\hat{f}$ is used as the error signal to update the variable filter $u(x,y,z)$. In the 3D context, the cost function used in the deconvolution procedure of the 3D image is defined as:

$$J(u) = J_1(u) + J_2(u) + \gamma\, J_3(u) \tag{2}$$

with,

$$J_1(u) = \sum_{(x,y,z)\in\mathcal{D}} \hat{f}^2(x,y,z)\left(\frac{1-\mathrm{sgn}(\hat{f}(x,y,z))}{2}\right)$$

$$J_2(u) = \sum_{(x,y,z)\in\overline{\mathcal{D}}} \left(\hat{f}(x,y,z) - L_{\mathrm{B}}\right)^2$$

$$J_3(u) = \Big(\sum_{\forall(x,y,z)} u(x,y,z) - 1\Big)^2$$

where $\hat{f}(x,y,z) = g(x,y,z) * u(x,y,z)$, and $\mathrm{sgn}(f) = -1$ if $f < 0$ and $\mathrm{sgn}(f) = 1$ if $f \geq 0$. $\mathcal{D}$ is the set of all pixels of $g(x,y,z)$ inside the region of support, and $\overline{\mathcal{D}}$ is the set of all pixels outside the region of support.

The first term, $J_1(u)$, is used to penalize the negative voxels in the support in order to keep the image estimate non-negative. The second term $J_2(u)$ penalizes voxels located outside the support which show values which deviate significantly from the background average L_{B}. When the background of the true image is black, i.e., $L_{\mathrm{B}} = 0$, the third term, $J_3(u)$, is used to avoid a trivial all-zero minimum solution (γ being a positive constant).

The authors have shown in [25] that the above equation is convex in the 2D case with respect to u. This property remains true in the 3D case so that convergence of the algorithm to the global minimum is ensured using the conjugate gradient minimization routine [25].

2.2. Anatomical Constraint 3D NAS-RIF

The major shortcoming of the NAS-RIF technique is its noise amplification at low SNR [1]. This is due to the high pass property of the inverse filter $u(x,y,z)$ which amplifies high frequency noise. As a result, the solution at convergence may not be the best estimate of the original image in the presence of noise. In order to solve this problem, a solution, suggested by Kundur and Hatzinakos [1], consists in halting the iterative restoration process through visual inspection. In practice, this requires a strong supervision and, even in this case, it is not so easy to determine which is the optimal iteration for termination (different parts of the image may converge at different rates, making this method unreliable).

In this work, we propose an alternative regularization approach for the NAS-RIF algorithm which can also be viewed as an elegant way to incorporate geometrical information extracted from a (high resolution) anatomical MR image into the SPECT data. The proposed regularization term also allows stabilization of the inverse solution by preventing noise amplification, does not require supervision (parameters tuning or stop criterion) and is capable of introducing better constraints on the solution of our restoration problem. This strategy consists in applying, over pre-detected and segmented anatomical regions, a piecewise smoothness constraint on the functional SPECT image to be recovered. To this end, our regularization term exploits the result of a preliminary registration step between the MR and SPECT image and also the result of a

segmentation of the MRI image into anatomical classes (cf. section 3).

In our model, the new cost function related to the deconvolution of the 3D image is now defined as:

$$J(u) = J_1(u) + J_2(u) + \gamma\, J_3(u) + \delta\, J_4(u) \tag{3}$$

with:

$$J_4(u) = \sum_{i=1}^{3} \sum_{(x,y,z)\in r_i} \Big(f(x,y,z) - \overline{r}_i \Big)^2$$

where the first summation is made on the three main "anatomical" types found in the brain, i.e., white matter ($r_{\mathbf{WM}}$), grey matter ($r_{\mathbf{GM}}$), and cerebro-spinal fluid ($r_{\mathbf{CSF}}$) and $\overline{r}_i$ designates the mean, in grey level, of the i^{th} region and δ is a weighting factor between this anatomical constraint and the hard constraints of the NAS-RIF procedure. In this context, $\mathcal{D} = r_{\mathbf{WM}} \cup r_{\mathbf{GM}} \cup r_{\mathbf{CSF}}$ and $\overline{r}_i = \frac{1}{N_{r_i}} \sum_{(x,y,z)\in r_i} \hat{f}(x,y,z)$ where N_{r_i} is the cardinal of the region r_i.

$J_4(u)$ is proportional to the sum of variance of each anatomical region (for each transversal slice) of the SPECT image. This term expresses that, within a detected and segmented anatomical region, pixels in the functional image should tend to have similar grey level values. This regularization term is edge-preserving since it allows to apply a smoothness constraint, while preserving (anatomical) discontinuities.

Furthermore, the introduction of this regularization term J_4 does not affect the convexity of the NAS-RIF cost function, and therefore a unique solution to the problem is still guaranteed. Fig. 2 shows the structure of this scheme. A preliminary registration step between the MR and SPECT image as well as the result of a segmentation of the MRI image into anatomical classes is used as the regularisation input to the error function.

The first derivative of the cost function in Eq. (3) is shown in Eq. (5). The gradient vector of J with respect to u is:

$$\nabla J(u) = \left(\begin{array}{ccccc} \frac{\partial J(u)}{\partial u(0,0,0)} & \cdots & \frac{\partial J(u)}{\partial u(i,j,l)} & \cdots & \frac{\partial J(u)}{\partial u(N_{xu}-1, N_{yu}-1, N_{zu}-1)} \end{array} \right)^T \tag{4}$$

where each entry is expressed as:

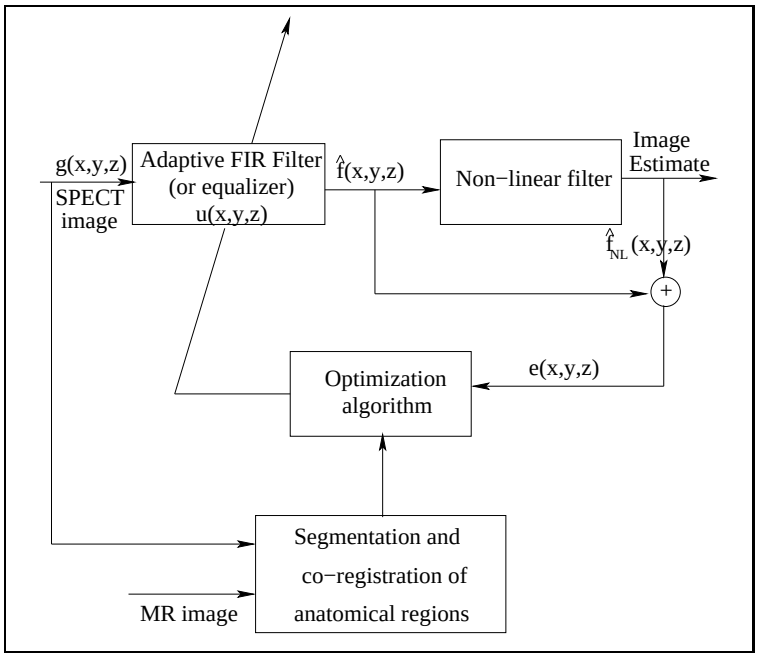

Figure 2: *Three-dimensional extension of the NAS-RIF deconvolution algorithm with incorporation of anatomical constraint.*

$$\begin{aligned}\frac{\partial J(u)}{\partial u(i,j,l)} &= 2\sum_{(x,y,z)\in\mathcal{D}} \hat{f}(x,y,z)\left(\frac{1-\mathrm{sgn}(\hat{f}(x,y,z))}{2}\right) g(x-i,y-j,z-l) + \\ &+ 2\sum_{(x,y,z)\in\overline{\mathcal{D}}} \big(\hat{f}(x,y,z) - L_{\mathrm{B}}\big) g(x-i,y-j,z-l) + \\ &+ 2\gamma\Big(\sum_{\forall(x,y,z)} u(x,y,z) - 1\Big) + \\ &+ 2\delta\sum_{n=1}^{3}\sum_{(x,y,z)\in r_n}\left(\hat{f}(x,y,z) - \frac{1}{N_{r_n}}\sum_{(x,y,z)\in r_n}\hat{f}(x,y,z)\right)\times \\ &\qquad\left(g(x-i,y-j,z-l) - \frac{1}{N_{r_n}}\sum_{(x,y,z)\in r_n} g(x-i,y-j,z-l)\right) \quad (5)\end{aligned}$$

A gradient-based iterative restoration algorithm or its conjugate version can be efficiently applied to minimize this convex cost function. Besides, since the proposed criterion is quadratic, many other optimization methods can be used.

The initial inverse FIR filter required by the NAS-RIF algorithm is the Kronecker delta

NAS-RIF Algorithm

Compute the filter coefficients $u(x, y, z)$ using a conjugate gradient optimization routine.

1. Definitions

l	The iteration step
t	A positive real number called the speed-gradient algorithm
$u^{[l]}$	Vector of filter of dimension $N_{xu} \times N_{yu} \times N_{zu}$ at the l^{th} iteration
$d^{[l]}$	Vector of dimension $N_{xu} \times N_{yu} \times N_{zu}$ at the l^{th} iteration
J	A cost function to be minimized
∇J	Gradient vector of J of dimension $N_{xu}N_{yu}N_{zu} \times 1$
$\langle ., . \rangle$	Scalar product

2. Initialization

$l = 0$
$u^{[0]} = (0 \cdots 1 \cdots 0)^T$
$d^{[0]} = -\nabla J(u^{[0]})$
Set speed-gradient algorithm $t > 0$

3. FIR filter parameters update

repeat

$\hat{f}(x, y, z) = g(x, y, z) * u(x, y, z)$

Calculate the gradient vector of J as indicated in Eq. (5)

if $l = 0$ **then**
$d^{[l]} = -\nabla J(u^{[l]})$
else
$\beta^{[l-1]} = \frac{\langle \nabla J(u^{[l]}) - \nabla J(u^{[l-1]}), \nabla J(u^{[l]}) \rangle}{\langle \nabla J(u^{[l-1]}), \nabla J(u^{l-1}) \rangle}$
$d^{[l]} = -\nabla J(u^{[l]}) + \beta^{[l-1]} d^{[l-1]}$

$u^{[l+1]} = u^{[l]} + t \times d^{[l]}$

$l = l + 1$;
until *a stopping criterion is met*;

Algorithm 1: *NAS-RIF Algorithm.*

function [25]; the size of this inverse filter is set to $3\times3\times3$ pixels. Furthermore, we have used $\gamma = 0$ because the background of SPECT images is not completely "black"[1].

Finally, the convergence criterion of the proposed algorithm is the stability of the cost function to be minimized, i.e.,

$$\frac{J(u^{[l+1]}) - J(u^{[l]})}{J(u^{[l]})} \leq \epsilon$$

with ϵ is a threshold, typically set, in our application to 10^{-3} and the upper-script denotes the iteration number. Fig. 3 shows the evolution of the cost function value along the iteration of the gradient descent process for the image restoration presented in Fig. 11.

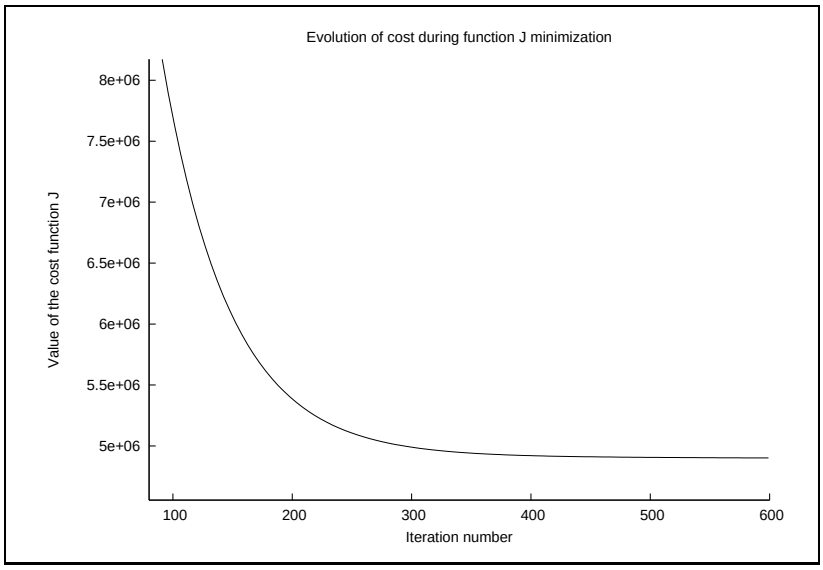

Figure 3: *Evolution of the cost function J along the iteration of the gradient descent process for an image restoration.*

3. REGISTRATION AND SEGMENTATION

In order to define our anatomically based regularization term J_4, we exploit the result of a 3D registration step between the MRI and SPECT input volumes (from the same patient) and then an unsupervised Markovian segmentation of the (registered) MRI 3D image into anatomical classes.

3.1. Registration

The 3D registration method used in our application is based on mutual information (MI) and is fully described in [26, 27]. The MI registration criterion $C(\theta)$ between the input MRI (I_{MRI}) and SPECT (I_{SPECT}) volumes is evaluated by

$$C(\theta) \;=\; \sum_{i} p_{I_{\text{MRI}}I_{\text{SPECT}}}(I_{\text{MRI}}(Hs), I_{\text{SPECT}}(s)) \;\log_2 \left(\frac{p_{I_{\text{MRI}}I_{\text{SPECT}}}(I_{\text{MRI}}(Hs), I_{\text{SPECT}}(s))}{p_{I_{\text{MRI}}}(I_{\text{MRI}}(Hs)) p_{I_{\text{SPECT}}}(I_{\text{SPECT}}(s))} \right) \quad (6)$$

where s is a voxel of the I_{SPECT} volume, $I_{\text{MRI}}(Hs)$ is the set of grey-values from the 3D image I_{MRI} sampled at the rigidly transformed coordinates Hs. H is the rigid transformation that describes a translation vector $T = (t_x, t_y, t_z)$ and a rotation vector $\alpha = (\alpha_x, \alpha_y, \alpha_z)$ (w.r.t. the x, y or z axis). θ is the registration parameter corresponding to the vector (α, T). Estimation of the marginal and joint image intensity distributions $p_{I_{\text{SPECT}}}(I_{\text{SPECT}}(s))$, $p_{I_{\text{MRI}}}(I_{\text{MRI}}(Hs))$, and $p_{I_{\text{MRI}}I_{\text{SPECT}}}(I_{\text{MRI}}(Hs), I_{\text{SPECT}}(s))$ are obtained by normalization of the joint and marginal histograms of the overlapping parts of both images I_{MRI} and I_{SPECT} [28]. To make coincide Hs with a grid point of I_{SPECT}, we have used trilinear interpolation to obtain samples from I_{SPECT}. The optimal registration parameter θ_{optimal} is then found by maximizing $C(\theta)$, where the vector θ is simply estimated by the Powell's method [29]. The scale is computed in advance because the voxel sizes of SPECT and MRI images are known and the images are initially positioned such that their centers coincide and that the corresponding scan axes of both images are aligned and have the same orientation. The images are smoothed slightly in order to make the cost function in Eq. (6) as smooth as possible to give faster convergence and less chance of finding bad local minima (related to a wrong registration). The code used to register the MRI image to the SPECT image is mainly inspired from the software package Statistical Parametric Mapping (SPM)[1].

3.2. Segmentation

To this end, we consider a couple of random fields $Z = (X, G)$, where $G = \{G_s, s \in S\}$ represents the field of observations located on the 3D lattice S consisting of K lattices S_k of N sites s (associated to the N pixels of each transversal slice of the brain 3D image), and $X = \{X_s, s \in S\}$ the label field (related to the $K \times N$ class labels X_s of a segmented 3D image). Each aforementioned

[1] The software package SPM can be obtained at : http://www.fil.ion.ucl.ac.uk/spm/

label is associated to a specific brain "tissue" category or region on the 3D image; the "CSF" and the area outside the brain are combined in a single class, corresponding to tissue without tracer uptake. Although, skin and other structures outside the brain actually have a non-zero (blood flow) tracer uptake. We assume this to be negligible here. The "CSF" area designates the regions that are normally devoid of activity. For this distribution mixture parameter estimation and segmentation problems, this region designates the brain regions filled with cerebro-spinal fluid (without blood flow and thus without radiation) and also the area outside the brain region. The "white matter" and "grey matter" (brightest region) are associated to lower and higher levels of blood flow respectively [30]. Each G_s takes its value in $\{0, \ldots, 255\}$ (256 grey levels), and each X_s in $\{e_1 =$"CSF", $e_2 =$"white matter", $e_3 =$"grey matter"$\}$.

In the following, the parameters in upper case letter designate the random variables whereas the lower case letters represent the realizations of those concerned random variables. The distribution of (X, G) is defined, firstly, by a prior distribution $P_X(x)$, hypothesized to be Markovian and secondly, by the site-wise conditional data likelihoods $P_{G_s/X_s}(g_s/x_s)$ whose shape and parameter vector $\Phi_{(x_s)}$ depends on the concerned class label x_s (g_s designates the grey level intensity associated to the site s). We assume independence between each random variable G_s given X_s. The observable G is called the "incomplete data" whereas Z constitutes the "complete data".

Estimation Step

In order to determine $\Phi = (\Phi_{(e_1)}, \Phi_{(e_2)}, \Phi_{(e_3)})$, we use the Iterative Conditional Estimation (ICE) algorithm [31] and the shape of the conditional likelihoods proposed in [23]. For the estimation and segmentation step of the MRI volume, we use Gaussian laws for the considered data likelihoods.

Segmentation Step

Based on the estimates given by the ICE procedure, we can compute an unsupervised 3D Markovian segmentation of the SPECT and MR volumes. In this framework, the Markovian segmentation can be viewed as a statistical labeling problem according to a global Bayesian formulation in which the posterior distribution $P_{X/G}(x/g) \propto \exp -U(x, g)$ has to be maximized [32]. The

corresponding posterior energy is:

$$U(x,g) = \underbrace{\sum_{s\in S} -\ln P_{G_s|X_s}(g_s \mid x_s)}_{U_1(x,g)} + \underbrace{\sum_{<s,t>} \beta_{st}\left(1-\delta(x_s,x_t)\right)}_{U_2(x)}$$

where U_1 expresses the adequacy between observations and labels, and U_2 represents the energy of the *a priori* model. $\beta_1, \beta_2, \beta_3$, such that $\beta_1 = \beta_2 = \beta_3 = \beta_{st}$, are called "the clique parameters" [32], and are associated to the horizontal, vertical, and transverse binary cliques[1] of our prior Pott model (which tends to favor homogeneous regions with no privileged orientation). We use the deterministic Iterated Conditional Modes (ICM) algorithm [32] to minimize this global energy function. For the initialization of this algorithm, we exploit the segmentation map obtained by a Maximum likelihood (ML) segmentation. In this segmentation, the "CSF", the "white matter" and the "grey matter" are represented by dark, grey, and white regions respectively, in order to visually express the activity levels of their blood flows. The support $\mathcal{D}$ is then determined simply by the set of pixels belonging to CSF, white and grey matter classes.

In order to take into account the Poisson noise phenomenon inherent to the SPECT imaging process in the "CSF" area, we use for the segmentation procedure and its estimation step an exponential law model [33]. We model the "white matter" and the "grey matter" regions, by two different Gaussian laws. For the MRI images, we model the "cerebrospinal fluid", the "white matter" and the "grey matter" regions, using again three different Gaussian laws.

4. VALIDATION

4.1. SPECT data acquisition and reconstruction

Cerebral blood flow studies were performed in this patient using ^{99m}Tc-ECD (Ethylene Cysteinate Dimer; Neurolite, DuPont; average dose: 34.2 MBq) and SPECT imaging. Acquisition was initiated approximately 45 minutes post intravenous injection of the radiopharmaceutical.

The SPECT images were acquired with a triple-head γ-camera (Picker Prism, Marconi Irix, Cleveland, OH) equipped with low-energy, high-resolution parallel-holes collimators. 90 projec-

[1] Cliques are subsets of sites which are mutual neighbors [32].

tions of 50 seconds each were obtained on $128 \times 128 \times N$ voxels with 1.85 mm isotropic voxels and $N \in [69, 103]$.

Two simultaneous acquisition windows were used, centered on 120 KeV and 140 KeV, both with a 15% width; the first one is used for Compton scattering correction (i.e., the Jaszczak method [34]), subtracting 40% of the activity in that window from that in the second, peak window, on a pixel by pixel basis. After this first correction, the resulting projections were filtered using a standard Butterworth filter (order of 8, cut off frequency of 0.39 cm^{-1}). This was followed by attenuation correction using a modified Chang algorithm (non-iterative). The maximum likelihood expectation maximization (ML-EM) reconstruction algorithm is then used to reconstruct projection data. It converges in approximately 16 iterations.

4.2. MRI data acquisition

The MRI images were acquired on a Siemens Magnetom Avanto 1.5T scanner using a 3D-FISP with a radial trajectory in k-space. It uses of a non-selective excitation. The scanning parameters are TR=9.2 ms, TE=22 ms with N slices of 512×512 voxels with voxel dimensions of 0.5×0.5×1.0 mm^3, and $N \in [130, 150]$. These 3D MRI images were further processed to isolate the brain from other tissues, using the brain extraction tool (BET) [35] of MRIcro[3] by adjusting BET's fractional intensity threshold.

4.3. Validation protocol on phantoms

Two phantoms were considered in order to validate the accuracy of our SPECT images restoration method:

- The Hoffman 3D Brain Phantom was scanned on both systems containing 148 MBq of activity. The phantom was positioned so that the slices within the phantom would match as well as possible by using the MR scout image to set the SPECT field of view to start at the top of the phantom for the studies on both systems. Phantom SPECT data included a set of 61 slices of 128×128 voxels with voxel dimension of $1.85 \times 1.85 \times 1.85$ mm^3. The Phantom MR data contained 209 slices of 256×256 voxels with 1 mm isotropic voxels. Fig. 4 shows a transversal slice of the Hoffman phantom.

[3]The software MRIcro can be obtained at : http://www.sph.sc.edu/comd/rorden/linux.html.

- The cylindrical phantom contains 6 different sphere sizes (whose diameters are respectively ♯1: 9.5 mm, ♯2: 12.7 mm, ♯3: 15.9 mm, ♯4: 19.1 mm, ♯5: 25.4 mm, ♯6: 31.0 mm). In one situation, the cylinder is filled with water and the spheres were filled with a Tc-99m solution with an activity concentration ratio of 2.7 : 1; in another situation, the cylinder is filled with a low activity Tc-99m solution and the spheres were filled with non radioactive water. Phantom SPECT data included a set of 93 slices of 128×128 voxels with voxel dimension of $1.85 \times 1.85 \times 1.85$ mm^3. The Phantom MR data contained 224 slices of 256×256 voxels with 1 mm isotropic voxels. Fig. 5 shows a transverse slice of the phantom (Deluxe ECT)[4].

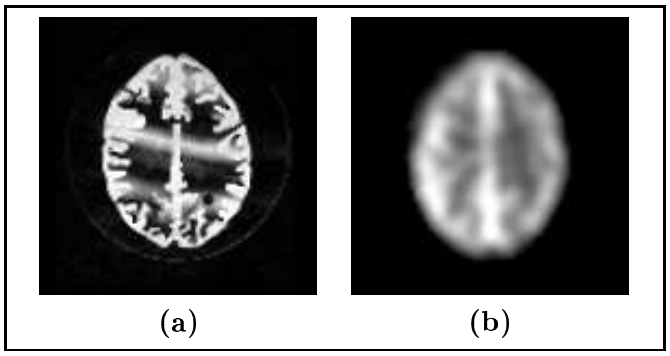

Figure 4: *Transverse slices of the Hoffman phantom.* **(a)** *MRI.* **(b)** *SPECT.*

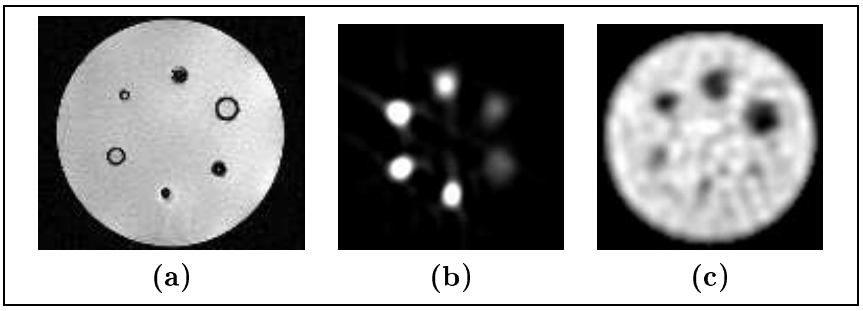

Figure 5: *Transverse slices of the cylindrical phantom.* **(a)** *MRI.* **(b)** *SPECT with hot spheres.* **(c)** *SPECT with cold spheres.*

Simple visual examination is an easy method for evaluation of the restorative power of a technique, but it is obviously an insufficient approach. A better evaluation approach consists in computing a performance measure based on the improvement in signal-to-noise ratio (ISNR),

[4]http://guillemet.org/irene/equipe4/fantomes.html.

expressed in decibels (dB), using both the degraded phantom, the ground truth (or the original undegraded image given by the MRI image), and the restored phantom images. The ISNR is defined by,

$$\text{ISNR} \;=\; 10\log\left(\frac{\|I_{ori}-I_{deg}\|^2}{\|I_{ori}-I_{res}\|^2}\right) \tag{7}$$

where I_{deg} is a given degraded phantom image, I_{ori} is the corresponding original (ground truth) phantom image and I_{res} is the restored phantom image. Obviously, this metric can only be used when the knowledge of the original image; in our case this will be given from the MRI phantom and the knowledge of the radioactivity concentration within each sub-compartment of the considered phantom.

In addition, restored images are also evaluated by the specific evaluation criteria proposed in [36] [37], based on the estimation of the four following measures:

(i) The global contrast [36] of the image, defined by $C_G = (1-m_{\mathbf{WM}}/m_{\mathbf{GM}})$, where $m_{\mathbf{WM}}$ and $m_{\mathbf{GM}}$ are the means of the pixel value in the "white matter" and "grey matter" areas respectively.

(ii) The local contrast of the image [37], defined by $C_L = (R_i - B_j)/B_j$, where R_i represents the mean grey level value inside the i^{th} sphere and B_j represents the mean grey level value outside the i^{th} sphere (in a circle centered around the sphere and whose radius D is half the distance from one sphere center to the next in the image.)

(iii) The image mottle $M_{\mathbf{WM}}$ in the "white matter" region [36], defined by $M_{\mathbf{WM}} = \sigma_{\mathbf{WM}}/m_{\mathbf{WM}}$, where $\sigma_{\mathbf{WM}}$ is the standard deviation of pixel values in this area.

(iv) The image mottle $M_{\mathbf{GM}}$ in the "grey matter" region [36], defined by $M_{\mathbf{GM}} = \sigma_{\mathbf{GM}}/m_{\mathbf{GM}}$, where $\sigma_{\mathbf{GM}}$ is the standard deviation of pixel values in this area.

These two parameters $M_{\mathbf{WM}}$ and $M_{\mathbf{GM}}$ allow to measure the amplification of the noise and/or measure the presence of undesirable artifacts that can be created by the restoration procedure in a uniform region of the SPECT volume. Due to the difference of proportion of pixels belonging to each brain anatomical tissue, we consider the total mottle measure given by $M = \rho_{\mathbf{WM}} M_{\mathbf{WM}} + \rho_{\mathbf{GM}} M_{\mathbf{GM}}$, with $\rho_{\mathbf{WM}}$ and $\rho_{\mathbf{GM}}$ designating the proportion of pixel belonging to the "white matter" and "gray matter" area respectively. A reliable SPECT image method restoration enhances then the image contrast with little increase in the mottle. Inversely, for a given maximal mottle measure, we can measure if the contrast enhancement is significantly increased [36].

4.4. Comparison with a supervised Metz restoration filter

We have compared our blind and unsupervised deconvolution approach with a classical deconvolution technique using the Metz filter [38]. The Metz filter is a supervised deconvolution (restoration) procedure which assumes the knowledge of the point spread function (PSF) of the imaging system. The filter is made up of the product of an inverse filter and a low pass filter. This filter allows to deconvolve the SPECT image while attenuating very high frequencies (i.e., artifacts which could be induced by the inverse filtering) [38].

5. EXPERIMENTAL RESULTS

5.1. Clinical data

Restoration with clinical data were performed on thirty pairs of MR and SPECT images from different epileptic patients. Each SPECT data set contained N slices of 128×128 voxels with voxel dimension of $1.85 \times 1.85 \times 1.85$ mm^3, and $N \in [69, 103]$. MRI data sets contained M slices of 512×512 voxels with voxel dimension of $0.5 \times 0.5 \times 1.0$ mm^3 and $M \in [130, 150]$. In this section, a few examples taken from that group will be presented.

Isolation of the brain (in MRI) from other tissues have been made *off-line* and not during the registration and restoration steps. BET's fractional intensity threshold is fixed to 0.50 in our application. This value has been chosen empirically after a set of tests.

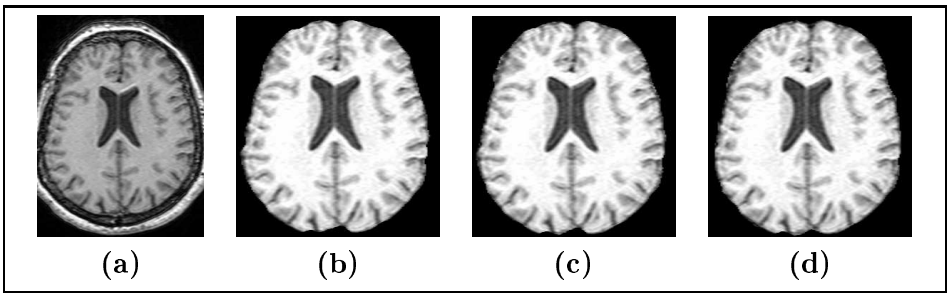

Figure 6: *Examples of brain extraction for different BET's fractional intensity threshold.* (**a**)*: Cross-section of a human brain MRI.* (**b**)*,* (**c**)*,* (**d**)*: Cross-section of the human brain isolated for different values for the BET's fractional intensity thresholds* 0.55*,* 0.50*,* 0.45 *respectively.*

Fig. 6 shows examples of brain extraction for different BET's fractional intensity thresholds.

An experimentation was then conducted in order to estimate the PSF of our SPECT imaging

	FWHM$_x(mm)$	FWHM$_y(mm)$	FWHM$_z(mm)$	σ_x	σ_y	σ_z
vial$_1$	9.50	9.05	11.00	4.03	3.84	4.67
vial$_2$	9.40	8.90	10.00	3.99	3.77	4.24

Table 1: FWHM and σ along the direction x, y, z for the two vials

system. To this end, a cylindrical phantom, filled with water and containing two very thin vials, filled with a Tc-99m solution (with an activity concentration of 173.9 and 148.0 MBq respectively) was constructed. Two PSFs, at two distances of the center of the cylindrical phantom, are generated from these radioactive source points from our SPECT imaging system. The most active vial is at the exact center of the cylindric phantom, and the other is 8 cm "off-axis".

Table 1 lists the full width at half maximum (FWHM) and the σ of the (assumed to be) Gaussian PSF along the direction x,y,z. The values of Table 1 are obtained by averaging over profiles along different directions. This table allows to observe that these two FWHM are nearly equals and thus that the blurring function is nearly invariant over a volume corresponding to a human brain volume. Consequently, our NAS-RIF model, which assumes a spatially-invariant blurring function is also justified.

We recall that the Metz filter has two parameter to be adjusted, FWHM and p (which is the order of the filter). In order to take into account the uncertainty of the measure of the FWHM of the PSF, we have simulated values around the ones estimated in Table 1 (namely 6.90, 7.88, 8.87, 10.84, 11.82, 12.81, 13.79 and 14.78 mm for FWHM) and several values for p (namely, 10, 20, 30, 40, 50, 70 and 80) for a total of 56 combinations of both parameters and we have taken the best ISNR value amongst these couples of parameters.

Fig. 7 shows the variation in ISNR of the processed phantom images w.r.t. the observations for a range of FWHM parameter and for the best value of p. By examining the ISNR for different values of FWHM, we notice that the optimal restoration value is for FWHM=9.85 mm, $p = 40$ corresponding to ISNR= 0.42 dB.

5.2. Registration and segmentation

Figure 8 shows original and segmented MRI cross-sections of human brain. Figure 9 shows example of registration of the MR volume with the SPECT volume (using MI registration method

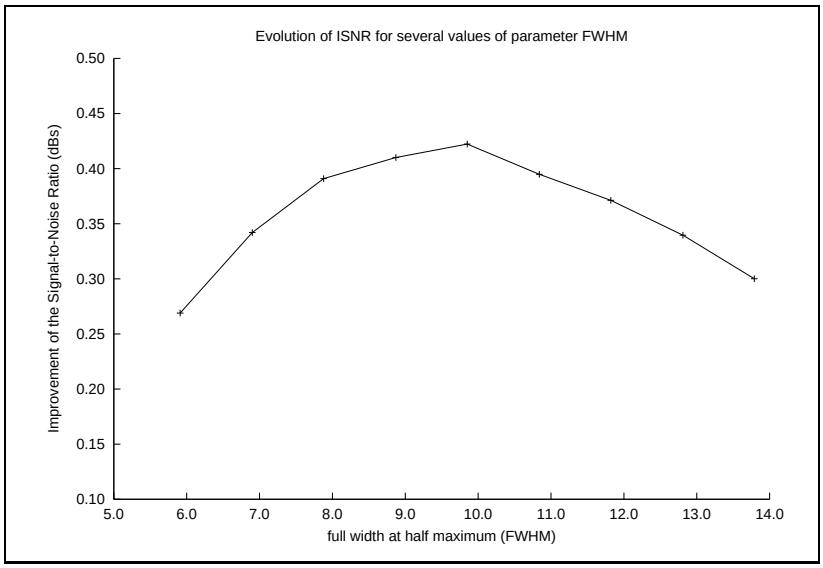

Figure 7: *ISNR as a function of the parameter $FWHM$ for the SPECT Hoffman phantom.*

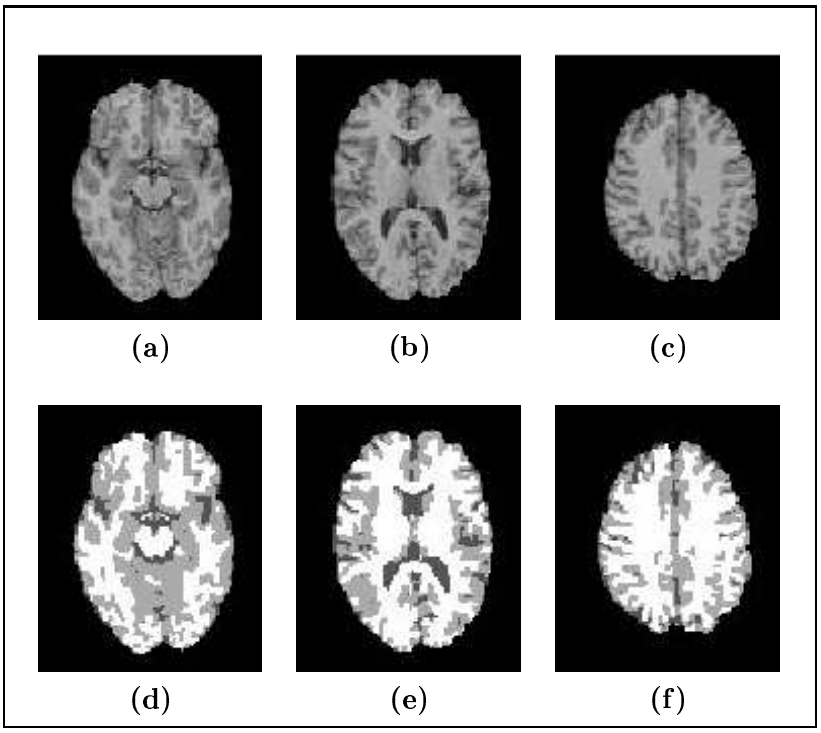

Figure 8: *Examples of segmentation of human brain MR volume.* **(a)(b)(c)***: Original MRI cross-sections.* **(d)(e)(f)***: Unsupervised 3D Markovian segmentations.*

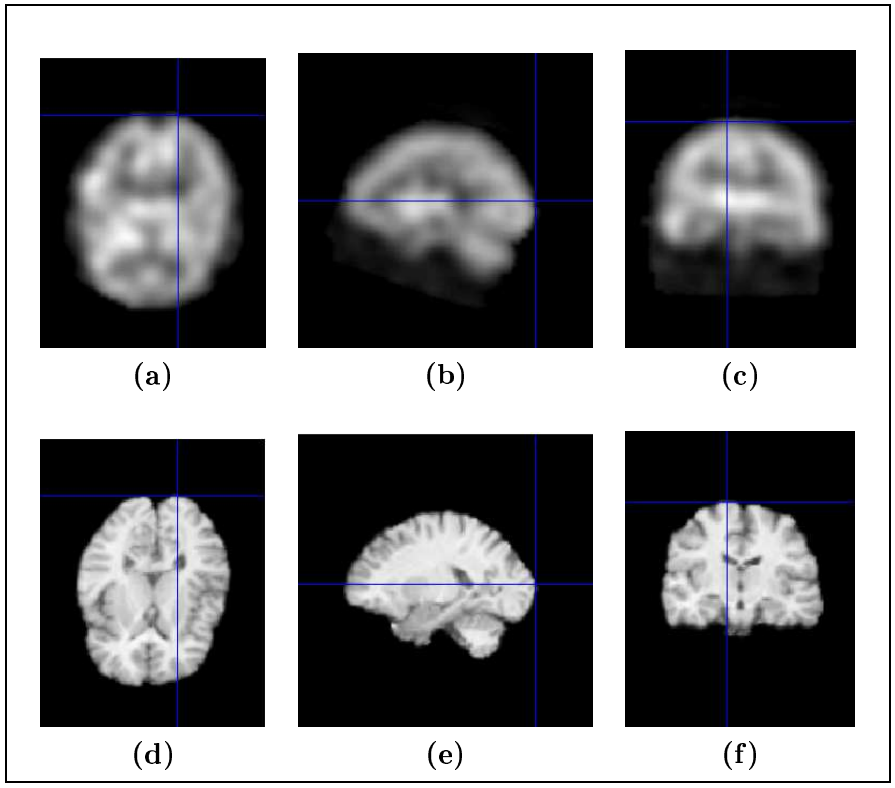

Figure 9: *Examples of registration of the MR volume to the SPECT volume (using registration method described in Section 3.1).* (**a**)(**b**)(**c**)*: Axial, sagittal, and coronal view of a SPECT volume.* (**d**)(**e**)(**f**)*: Axial, sagittal, and coronal view of a registered MR volume.*

	Restored images			Degraded images
	with $J_4(u)$	Metz filter	without $J_4(u)$	
Contrast C_G	37.3	30.4	24.3	20.0
Mottle M	14.1	13.0	12.1	12.1

Table 2: The global contrast and total mottle (expressed in %) obtained from respectively the restored image with and without $J_4(u)$, the Metz filter, and the degraded images, that are the original real SPECT images.

Phantoms	Restored images									Degraded images	
	with $J_4(u)$			Metz filter			without $J_4(u)$				
	C_G	M	$ISNR$	C_G	M	$ISNR$	C_G	M	$ISNR$	C_G	M
Hoffman	30.4	25.2	0.7	23.0	20.1	0.4	19.2	17.8	0.3	18.2	17,4
Cold spheres	28.2	36.4	0.7	20.7	32.3	0.4	19.5	26.5	0.2	17.0	26.0
Hot spheres	27.8	38.7	0.7	20.1	33.1	0.4	19.0	27.4	0.2	16.3	26.4

Table 3: The global contrast C_G and the mottle M (expressed in %) and the improvement signal-to-noise ratio $ISNR$ (expressed in dB) obtained from respectively the restored image with and without $J_4(u)$, the Metz filter, and the degraded images that are the original phantom SPECT.

described in Section 3.1).

5.3. Quantitative results

Average contrast and total mottle were first quantified on a set of (human brain) SPECT degraded and restored images (with and without our anatomical-based regularization term $J_4(u)$) and compared to the Metz filter. The results are shown in Table 2. Our proposed algorithm with $J_4(u)$ allows to increase the global contrast by 1.87 and the mottle by a factor of 1.17. The Metz filter allows to increase the global contrast by 1.52 and the mottle by a (somewhat similar) factor of 1.08.

On SPECT phantom, the results are now shown in Table 3 and give similar results. When compared with a classical restoration approach using a Metz filter, our method thus performs better, in terms of signal-to-noise ratio. The increase of the mottle with J_4 is a little price to pay given the gain in global contrast, ISNR, and local contrast measures, which from a

Cold Sphere$_i$	1	2	3	4	5	6
C_L (with partially incorrect anatomic information)	22.7	20.0	17.3	14.6	10.6	5.6
C_L (with correct anatomic information)	23.3	19.5	15.9	14.8	9.4	6.9

Table 4: Local contrast C_L (expressed in %) with and without correct anatomic information obtained from the restored image with $J_4(u)$

Cold Sphere$_i$	Restored images			Degraded
	with $J_4(u)$	Metz filter	without $J_4(u)$	image
	C_L	C_L	C_L	C_L
1	23.3	17.2	16.1	14.4
2	19.5	16.7	14.9	12.1
3	15.9	12.3	11.2	9.3
4	14.8	10.4	9.0	7.8
5	9.4	7.1	6.0	4.1
6	6.9	4.6	3.1	2.1

Table 5: The local contrast C_L (expressed in %) with correct anatomic side information obtained from respectively the restored image with and without $J_4(u)$, the Metz filter, and the degraded image that are the original phantom SPECT.

clinical perspective ensures better detection of focal anomalies, a task at which SPECT is usually notoriously poor.

SPECT image with cold spheres were also restored using partially incorrect anatomic information (i.e., cylindrical phantom MRI with 5 different sphere sizes instead of 6; one segmented sphere was removed in the MRI segmented image). Table 4 shows that the local contrast measured on this restored SPECT image (with our anatomical-based regularization term $J_4(u)$) remains similar with local contrast obtained with correct anatomic information. This test shows that the restored image is constrained (or guided) by our prior knowledge but not wrongly biased by this information.

In this experiment, the "the support constraint" energy term, acting as a likelihood energy term, allows to counterbalance the locally wrong information given by the prior energy term $J_4(u)$.

Local contrast was quantified on individual spheres of SPECT degraded and restored images (with and without our anatomical-based regularization term $J_4(u)$) and compared to the Metz filter. Table 5 shows that our proposed algorithm with $J_4(u)$ allows to increase in average the local contrast by 2.10. The Metz filter allows to increase in average the local contrast by 1.53.

5.4. Example of restoration

Figure 11 present example of brain SPECT volumes restoration obtained with our restoration method. The restoration of a whole brain converges to a very good estimate of the solution without *a priori* information about the PSF and allows to noticeably improve the resolution of the original SPECT volume. This restoration could allow efficient detection of small, localized singularities associated with different types of lesion (tumors, epileptogenic foci, etc.) that often are not clearly visible in the original blurred image.

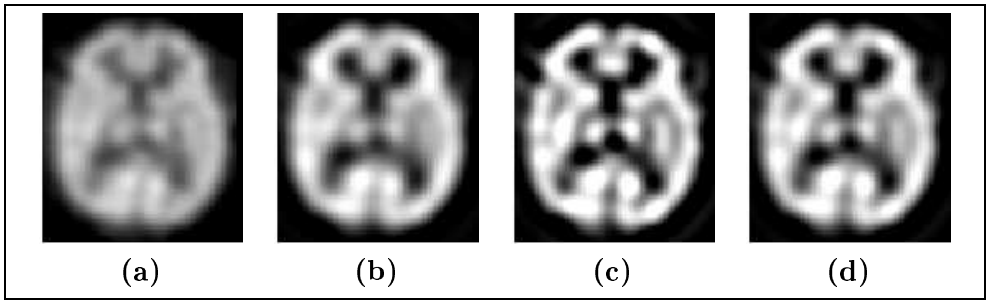

Figure 10: *Examples of different restoration results using different support.* (**a**)*: Axial view of brain SPECT volume.* (**b**)(**c**)(**d**)*: different restoration results given by our anatomical constraint version of the NAS-RIF algorithm using different support given in Fig.6*

One can easily notice that this SPECT volume is less noisy and less blurred than the clinical human brain SPECT volumes previously presented and processed. This is due to several factors, such as different radioactivity concentrations within the different, uniform regions of this SPECT phantom, a longer acquisition time, the complete absence of motion of this simulated brain during SPECT acquisition (which is only rarely achieved with patients), reduced attenuation, etc. This actually suggests that improvements in the signal-to-noise ratio obtained with our method on real brain images should be greater than 0.72 dB.

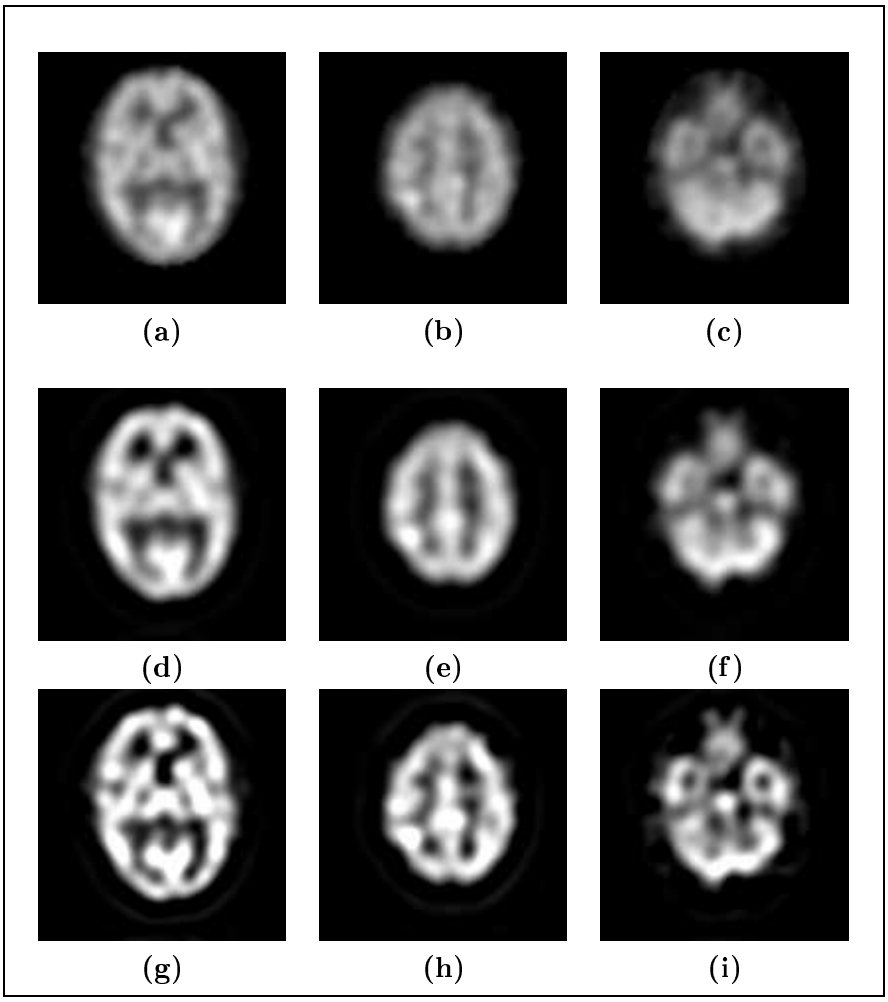

Figure 11: *Examples of deconvolutions obtained by our method and Metz filter on cross-sectional slices from SPECT images.* (**a**)(**b**) *and* (**c**)*: Original SPECT cross-sectional phantom images.* (**d**)(**e**) *and* (**f**)*: deconvolution result with Metz filter.*(**g**)(**h**) *and* (**i**)*: deconvolution result with our method.*

5.5. Discussion

Fig.10 shows examples of different restoration results of our method using different value of the BET's fractional intensity threshold (giving different isolation of the brain from other tissues (see Fig.6)). Our restoration procedure is not very sensitive to this threshold value when it is visually set by an experimented user (for instance the value of contrast is stationary when the threshold goes from 0.45 to 0.55). Nevertheless, this parameter was easily set to 0.50 once and for all the thirty pairs of MR images and seems to be optimal in all tested cases. This threshold is easy to set visually.

The PSF estimated by our method (in fact, the Fourier inverse of our NAS-RIF inverse filter) along the direction x,y and z can be approximated by a Gaussian distribution with standard deviations equal to 3.58, 3.10 and 3.31 along the x, y and z axes (this corresponds to 8.45, 7.31, and 7.78 mm FWHM respectively). When we compare this PSF with the one experimentally used with the Metz filter, we can note the similarity between these two results.

Our method will work best with agents showing a widespread brain distribution and well delineated grey and white matters such as observed with blood flow tracers (99mTc labeled HMPAO or ECD).

The computational time of our technique takes approximatively 6.33 minutes against 0.24 minutes for the Metz filter on a 2.0 GHz PC workstation running Linux. Our method is computationally demanding but recall that our method is blind and does not require any parameters of the PSF function.

Among the disadvantages of our method, we can cite its computational cost due to its iterative nature and the need of an additional MRI scan. Also, the accuracy of the registration procedure is crucial for the final restoration result.

6. CONCLUSION

In this paper, we have presented a robust, post-reconstruction restoration method of 3D SPECT images. This method improves the resolution of human brain 3D SPECT images and should thus be helpful to physicians interpreting such studies. Our approach takes advantage of the anatomical and geometrical information contained in the MRI study of each subject. The pro-

posed constraint term allows both stabilization of the inverse solution of the NAS-RIF procedure by prevention of noise amplification and the generation of a better constraint on the solution of our restoration problem. In the regularization framework, this term allows smooth regions to be reconstructed in the SPECT image, where such homogeneous anatomical regions are found in the high resolution MRI images of the patient, after those have been registered to the subject's SPECT volume. This method has been tested on a number of SPECT/MR pairs, demonstrating its efficiency and robustness. This 3D blind restoration technique is completely data driven, and could be implemented to automatically process massive numbers of 3D SPECT studies.

References

[1] D. Kundur and D. Hatzinakos. A novel blind deconvolution scheme for image restoration using recursive filtering. *IEEE Transactions on Signal Processing*, 46(2):375–390, 1998.

[2] P. Calvini, A.M. Massone, F.M. Nobili, and G. Rodriguez. Fusion of the MR image to SPECT with possible correction for partial volume effects. *IEEE Transactions on Nuclear Science*, 53(1):189–197, 2006.

[3] C. A. Bouman and K. Sauer. A unified approach to statistical tomography using coordinate descent optimization. *IEEE Transactions on Image Processing*, 5(3):480–492, 1996.

[4] S. Alenius, U. Ruotsalainen, and J. Astola. Using local median as the location of the prior distribution in iterative emission tomography image reconstruction. *IEEE Transactions on Nuclear Science*, 45(6):3097–3104, 1998.

[5] S.C. Moore, M.F. Kijewski, S.P. Müller, F. Rybicki, and R.E. Zimmerman. Evaluation of scatter compensation methods by their effects on parameter estimation from SPECT projections. *Medical Physics*, 28(2):278–287, 2001.

[6] D.C. Vines, M. Ichise, J.S. Liow, H. Toyama, and R.B. Innis. Evaluation of 2 scatter correction methods using a striatal phantom for quantitative brain SPECT. *Journal of Nuclear Medicine Technology*, 31(3):157–160, 2003.

[7] G. El Fakhri, J. Ouyang, R.E. Zimmerman, A.J. Fischman, and M.F. Kijewski. Performance of a novel collimator for high-sensitivity brain SPECT. *Medical Physics*, 33(1):209–215, 2006.

[8] W. Römer, N. Reichel, H.A. Vija, I. Nickel, J. Hornegger, W. Bautz, and T. Kuwert. Isotropic reconstruction of SPECT data using OSEM3D: Correlation with CT. *Academic Radiology*, 13(4):496–502, 2006.

[9] S.C. Moore, J. Ouyang, Mi-Ae Park, and G. El Fakhri. Monte carlo-based compensation for patient scatter, detector scatter, and crosstalk contamination in in-111 SPECT imaging. In *Nuclear Instruments and Methods in Physics Research*, volume 569, pages 472–476, December 2006.

[10] H.W.A.M. De Jong, E.T.P. Slijpen, and F.J. Beekman. Acceleration of monte carlo SPECT simulation using convolution-based forced detection. *IEEE Transactions on Nuclear Science*, 48(1):58–64, 2001.

[11] W.G. Hawkins, P.K. Leichner, and N.-C. Yang. The circular harmonic transform for SPECT reconstruction and boundary conditions on the fourier transform of the sinogram. *IEEE Transactions on Medical Imaging*, 7(2):135–138, 1988.

[12] S.J. Glick, B.C. Penney, M.A. King, and C.L. Byrne. Noniterative compensation for the distance-dependent detector response and photon attenuation in SPECT imaging. *IEEE Transactions on Medical Imaging*, 13(2):363–374, 1994.

[13] A.W. McCarthy and M.I. Miller. Maximum likelihood SPECT in clinical computation times using mesh-connected parallel computers. *IEEE Transactions on Medical Imaging*, 10(3):426–436, 1991.

[14] V. Kohli, M.A. King, S.J. Glick, and T.-S. Pan. Comparison of frequency-distance relationship and gaussian-diffusion-based methods of compensation for distance-dependent spatial resolution in SPECT imaging. *Physics in Medicine and Biology*, 43:1025–1037, 1998.

[15] G. Gindi, M. Lee, A. Rangarajan, and I. G. Zubal. Bayesian reconstruction of functional images using anatomical information as priors. *IEEE Transactions on Medical Imaging*, 12(4):670–680, 1993.

[16] C.-T. Chen, X. Ouyang, W. H. Wong, X. Hu, and V. E. Johnson. Sensor fusion in image reconstruction. *IEEE Transactions on Nuclear Science*, 38(2):687–691, 1991.

[17] R. Leahy and X. Yan. Incorporation of anatomical MR data for improved functional imaging with PET. In *Information Procesing in Medical Imaging (Lecture Notes in Computer Science 511)*, pages 105–120, 1991.

[18] X. Ouyang, W. H. Wong, V. E. Johnson, X. Hu, and C. T. Chen. Incorporation of correlated structural images in PET image reconstruction. *IEEE Transactions on Medical Imaging*, 13(4):627–640, 1994.

[19] B. Lipinski, H. Hertzog, E. R. Kops, W. Oberschelp, and H. W. Muller-Gartner. Expectation maximization reconstruction of positron emission tomography images using anatomical magnetic resonance information. *IEEE Transactions on Medical Imaging*, 16(2):129–136, 1997.

[20] S. Sastry and R. E. Carson. Multimodality Bayesian algorithm for image reconstruction in Positron Emission Tomography: a tissue composition model. *IEEE Transactions on Medical Imaging*, 16(6):750–761, 1997.

[21] J. Nuyts, K. Baete, D. Beque, and P. Dupont. Comparison between MAP and postprocessed ML for image reconstruction in emission tomography when anatomical knowledge is available. *IEEE Transactions on Medical Imaging*, 24(5):667–675, 2005.

[22] H. Rajabi, A. Bitarafan Rajabi, N. Yaghoobi, H. Firouzabad, and F. Rustgou. Determination of the optimum filter function for tc99m-sastamibi myocardial perfusion SPECT imaging. *Indian Journal of Nuclear Medicine*, 20(3):77–82, 2005.

[23] M. Mignotte and J. Meunier. Three-dimensional blind deconvolution of SPECT images. *IEEE Transactions on Biomedical Engineering*, 4(2):274–281, 2000.

[24] S. Benameur, M. Mignotte, J. Meunier, and J-P Soucy. An edge-preserving anatomical-based regularization term for the NAS-RIF restoration of SPECT image. In *13th IEEE International Conference on Image Processing*, pages 1177–1180, Atlanta, GA, USA, October 2006.

[25] D. Kundur and D. Hatzinakos. Blind image restoration via recursive filtering using deterministic constraints. In *Proc. International Conference on Acoustics, Speech, and Signal Processing*, volume 4, pages 547–549, 1996.

[26] A. Collignon, F. Maes, D. Delaere, D. Vandermeulen, P. Suetens, and G. Marchal. Automated multi-modality image registration based on information theory. In *Information Processing in Medical Imaging Conference*, pages 263–274, 1995.

[27] W.M. Wells, P. Viola, H. Atsumi, S. Nakajima, and R. Kikinis. Multi-modal volume registration by maximization of mutual information. *Medical Image Analysis*, 1(1):35–51, 1996.

[28] C. Studholme, D.J. Hawkes, and D.L. Hill. Normalized entropy measure for multimodality image alignment. In *Medical Imaging, Image Processing, Kenneth M. Hanson; Ed.*, volume 3338, pages 132–143, June 1998.

[29] M.J.D. Powell. An eeficient method for finding the minimum of a function of several variables without calculating derivatives. *Computer Journal*, (7):152–162, 1964.

[30] D.C. Costa and P.J. Ell. *Brain Blood Flow in Neurology and Psychiatry.* Series Editor: P.J. Ell, 1991.

[31] F. Salzenstein and W. Pieczinsky. Unsupervised Bayesian segmentation using hidden Markovian fields. In *International Conference on Acoustics, Speech, and Signal Processing*, volume 4, pages 2411–2413, Detroit, May 1995.

[32] J. Besag. On the statistical analysis of dirty pictures. *Journal of the Royal Statistical Society*, B-48:259–302, 1986.

[33] T.S. Curry, J.E. Dowdey, and R.C. Murry. *Christensen's Physics of Diagnostic Radiology.* Lea and Febiger, 1990.

[34] R. Jaszczak, C. Floyd, and R. Coleman. Scatter compensations techniques for SPECT. *IEEE Transactions on Nuclear Science*, 32:786–793, 1985.

[35] S.M. Smith. Fast robust automated brain extraction. *Human Brain Mapping*, 17(3):143–155, 2002.

[36] S. Webb, A.P. Long, R.J. Ott, M.O. Leach, and M.A. Flower. Constrained deconvolution of SPECT liver tomograms by direct digital image restoration. *Medical Physics*, 12(1):53–58, 1985.

[37] A.H. Vija, E.G.Hawman, and J.C. Engdahl. Analysis of a spect osem reconstruction method with 3D beam modeling and optional attenuation correction: phantom studies. In *IEEE Medical Imaging Conference Proceedings*, pages 2662–2667, October 16-22, 2004.

[38] C.E. Metz and R.N. Beck. Quantitative effects of stationary linear image processing on noise and resolution of structure in radionuclide images. *The Journal of Nuclear Medicine*, 15(3):164–170, 1974.